The Circular Cylinder in Subsonic and Transonic Flow

O. Rodriguez*
Institut de Mécanique des Fluides de Lille, Lille, France

This paper provides new results describing compressible fluid flow around a cylinder. The investigation was restricted to subsonic and transonic flow at Reynolds numbers of about 10^5. The experiments showed that a strong coupling exists between the flow over a cylinder and the vortex street formed in the near wake. The phenomenon was investigated using high-speed visualization synchronized with unsteady pressure measurements. Various coupling regimes were classified and instantaneous pressure distributions were obtained at different times during the vortex street period. From these elements it was possible to deduce the unsteady force.

Introduction

THE flow around a cylinder has already been investigated intensively. A number of published papers have been concerned with incompressible flow, the results of which have been summarized in a recent review by C. Farell.[1] However, studies dealing with compressible flows are scarce. Velocities corresponding to Mach numbers of about 0.3 have been reached in experiments conducted at very high Reynolds numbers.[2,3] Of the studies devoted particularly to the subsonic and transonic ranges, one can cite the pioneer paper by Nauman et al.[4] as well as the results obtained by Murthy and Rose[5] in the Mach 0.25-1.2 range. Consequently, incompressible flows past a cylinder are known quite well, but experimental data for high-speed flows remain sparse and incomplete.

It was formerly thought that the disturbances issuing from the wake could be regarded as a perturbation field superimposed upon the continuous velocity field. But over the last few years, numerous studies have proved the existence of a coupling between the flow on the body and the vortex street. Visualization[6-9] indicates that at subsonic speeds the coupling increases with the upstream Mach number M_∞. The coupling appears as a regular oscillation of the separation points; visualization has verified that the oscillation has the same frequency N as the vortex street. The coupling decreases above the critical Mach number. This property has been explained by the possibility of an upstream transmission of the disturbances created by the vortex street.[6,9] When the supersonic pockets are bounded, the upstream influence can pass both around the top of the shock wave and through the recirculating zone. At larger Mach numbers, the shocks extend further out; the disturbances can be transmitted upstream only through the subsonic part of the recirculating field and this part becomes smaller as M_∞ increases. Above a given value of M_∞, there are two λ shocks, the extremities of which nearly come into contact so that communication between the vortex street and the near wake is cut off. Consequently, the whole field situated upstream of the shock waves becomes independent of the vortex street; that is, it becomes quasisteady. This explains why measurements made on the body in this regime did not detect the existence of a vortex street.[5]

The use of high-speed visualization has enabled researchers to estimate the vortex street Strouhal number. This number is almost independent of M_∞ and approximately equal to 0.2 for Reynolds numbers of $0.8\text{-}2\times10^5$, except for a sudden rise when the quasisteady regime is reached. In this regime, the size of the body no longer represents the characteristic length of the vortex street. Assuming that this length is now the distance between the extremities of the two shock waves and that the Strouhal number can be based upon the new length, we once again arrive[6,9] at a value close to 0.2.

Experimental Setup

The experiments were conducted in a continuous closed-circuit wind tunnel with test section dimensions of 42×200 mm^2. The stagnation pressure was atmospheric and the stagnation temperature was kept close to room temperature by means of an air exchange system. The floor and ceiling were equipped with longitudinal adjustable permeability slots. A sonic throat downstream from the test section was used to stabilize the flow. The turbulence level was about 0.5% at Mach 0.5. Shadowgraphs and schlieren visualizations were made with a 24 spark Cranz-Schardin system, the duration Δt between two successive sparks being adjustable. This device enabled us to record the time history of the observed phenomenon and thus obtain measurements of the frequencies and speeds of propagation. The time interval Δt was chosen so that at least one period of the vortex street would be covered by the 24 pictures.

Tests were made with a cylinder 20 mm in diameter. The model used for these experiments had one fixed and one movable part, each equipped with a pressure tap and a flush-mounted pressure transducer, both of which were located on the same generatrix. The fixed pressure transducer was situated at azimuth -30 deg. The movable part could be rotated from -30 to 190 deg (Fig. 1). A photocell detected the 24 visualization sparks, which, together with the transducer's signals, were recorded on a magnetic tape.

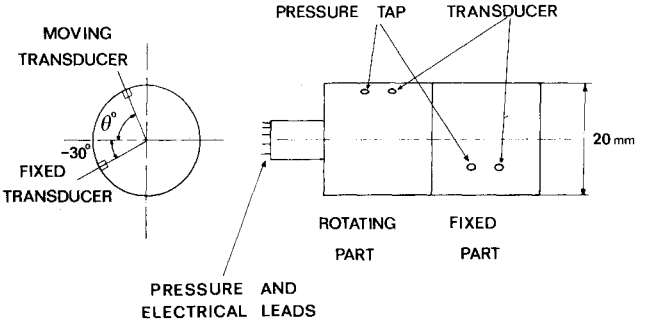

Fig. 1 Schematic of cylinder model.

Received April 6, 1983, revision received Dec. 27, 1983.

*Research Engineer.

This arrangement presented certain weaknesses:

1) In spite of the slotted walls and the moderate height of the model, there was interference with the walls, especially at Mach numbers close to 1.

2) The test section was narrow and the sidewall boundary layers therefore had some influence on the flow.

3) The Reynolds and the Mach numbers could not be modified independently. The range of variation of the Reynolds number was $1.7\text{x}10^5 \leq Re \leq 3.4 \times 10^5$. This fact does not seem to be of importance, however, because the steady pressure distribution curves show that the separation is always laminar.

4) The transducers were relatively large compared with the diameter of the cylinder; the corresponding inscribed angle was about 4.5 deg.

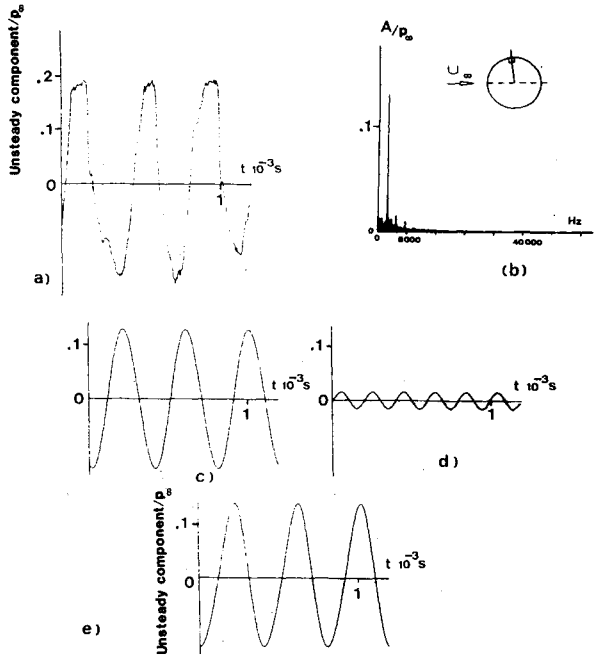

Fig. 2 Modeled signal for $M_\infty = 0.75$ and $\theta = 85$ deg: a) recorded signal, b) Fourier spetrum, c) fundamental, d) first harmonic, e) modeled signal (p_∞ is the upstream pressure and A the amplitude of the fundamental component of the unsteady pressure).

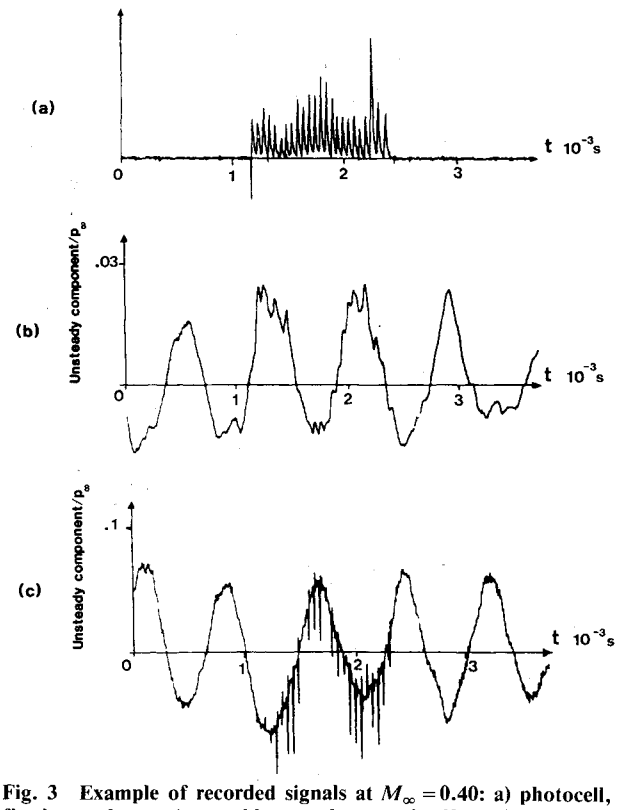

Fig. 3 Example of recorded signals at $M_\infty = 0.40$: a) photocell, b) fixed transducer, c) movable transducer at $\theta = 65$ deg (p_∞ is the upstream pressure).

Unsteady Pressure Data Processing

Following digitization, a spectral analysis of the pressure signals was performed by a fast Fourier transform (FFT) from the data samples. The frequency resolution thus obtained was 40 Hz and the bandwith 80 kHz.

Figure 2 shows the signal transmitted by the movable transducer at the 85 deg azimuth and the corresponding frequency spectrum for $M_\infty = 0.75$. Two peaks are dominant: a fundamental component and its first harmonic, the intensity of which is noticeably weaker. The other components originate from freestream turbulence and from the perturbation generated by such parameters as electric noise, the motor itself, and the visualization system.

This result corroborates the periodic nature of the phenomenon previously shown by visualization. The pressure signals can therefore be modeled as the sum of the fundamental component and its first harmonic, thus filtering extraneous noise. Similar results were obtained in subsonic flow at $M_\infty = 0.40$ and 0.55. Since the pressure signals and the photocell signal were recorded simultaneously, the pressure measured by the fixed transducer is known for every picture (Fig. 3). For a chosen test, let us call ϕ_0 the phase of this signal at the first picture. For every azimuth, the phase of the movable transducer signal can be determined when the fixed

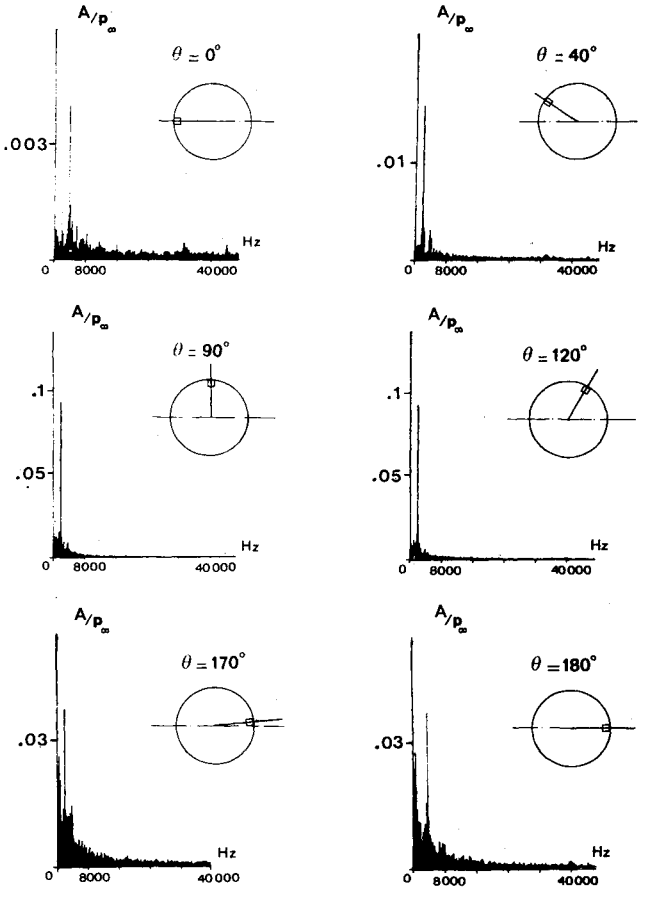

Fig. 4 Fourier spectra at $M_\infty = 0.55$ (p_∞ is the upstream pressure and A the amplitude of the fundamental component of the unsteady pressure).

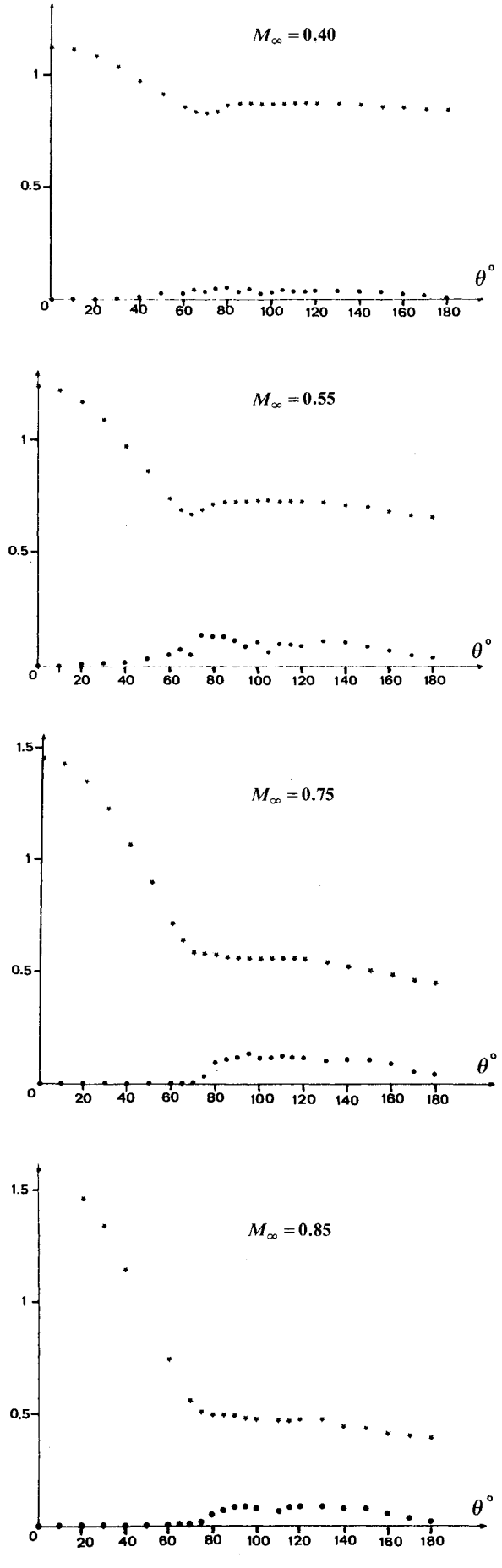

Fig. 5 Pressure distribution: *mean pressure (p/p_∞), • intensity of the fundamental component of the unsteady pressure (A/p_∞).

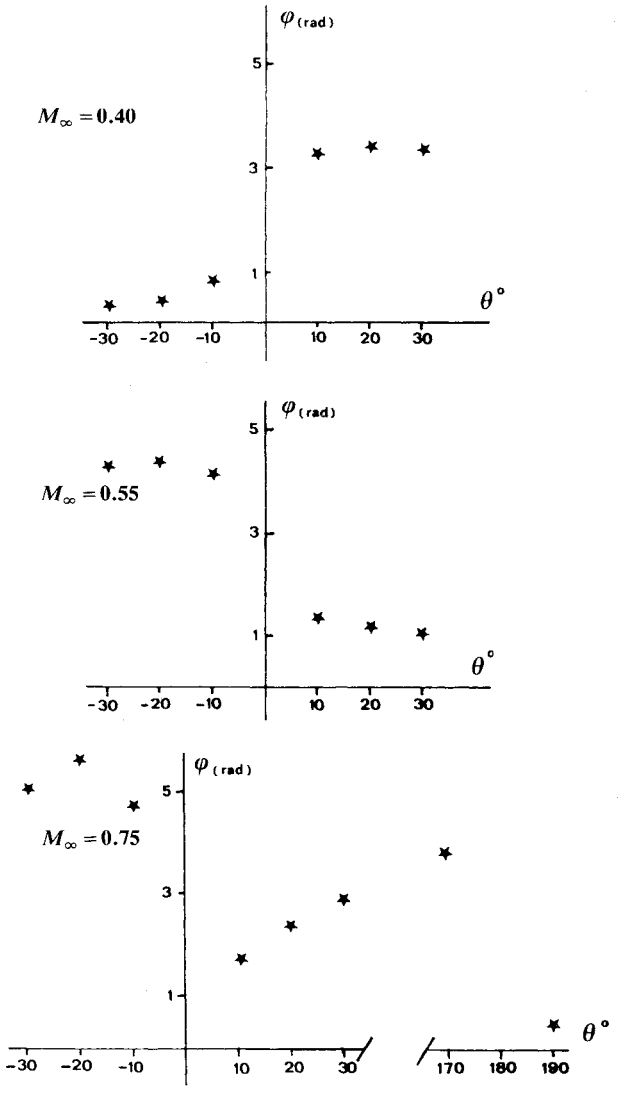

Fig. 6 Phase of the fundamental component.

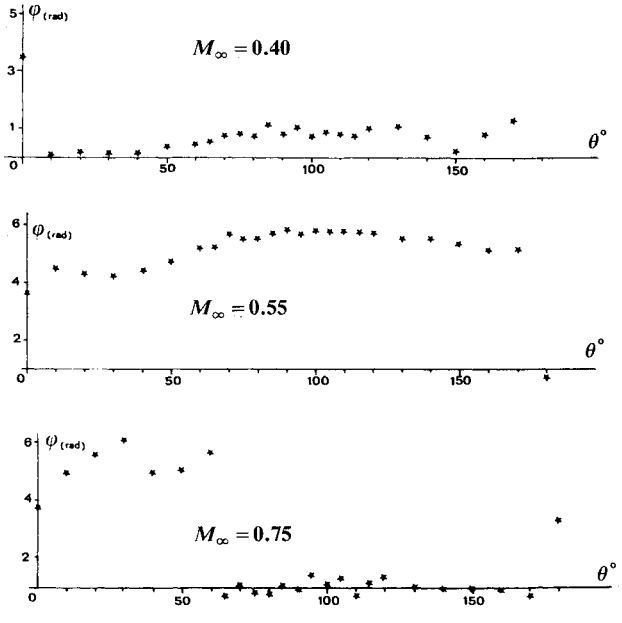

Fig. 7 Phase of the recorded signal transmitted by the movable transducer.

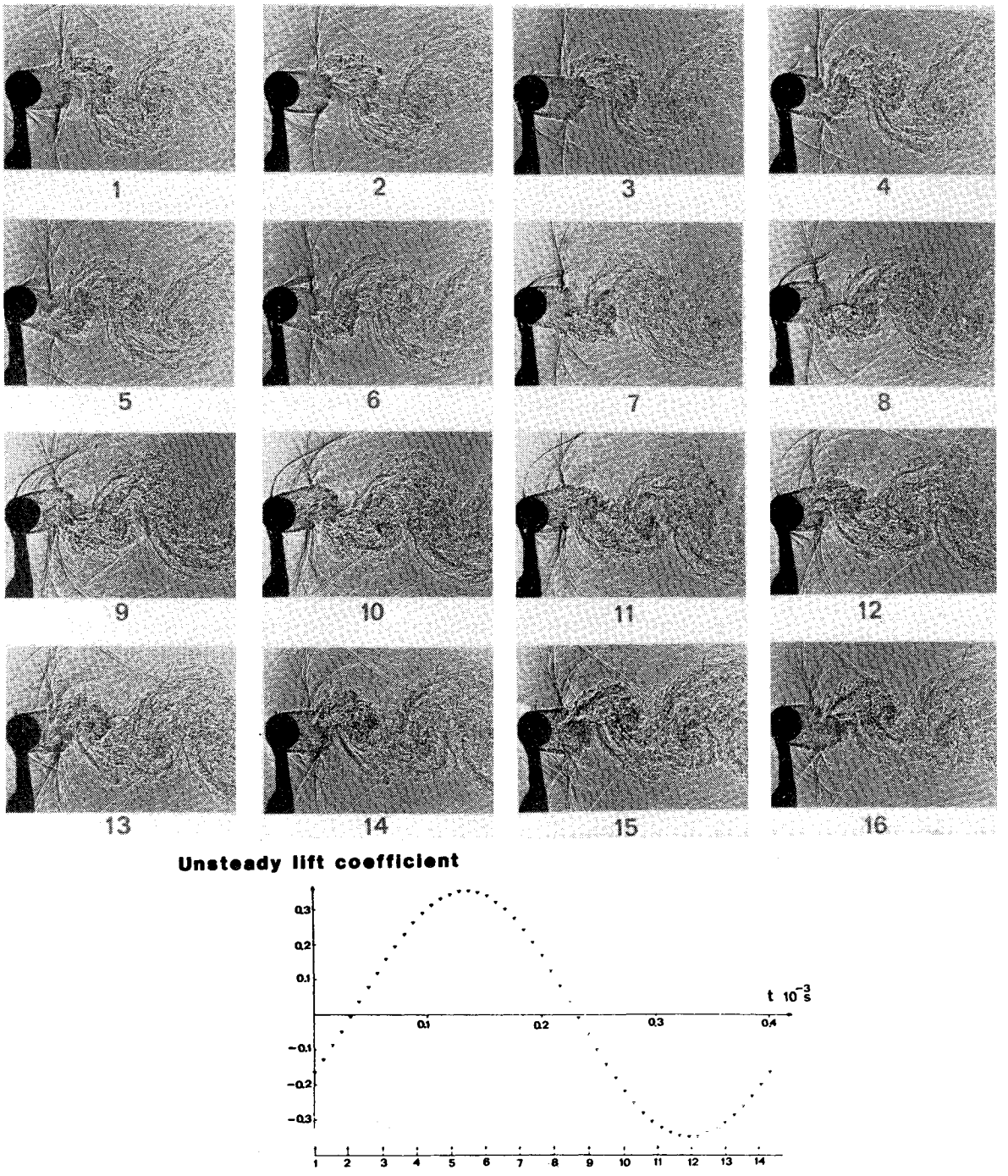

Fig. 8 Visualizations and lift for $M_\infty = 0.75$ and $\Delta t = 0.30$ μs.

transducer phase reaches ϕ_0. The instantaneous pressure distribution between azimuths -30 and 190 deg corresponding to the first picture can thus be obtained and, due to the periodic character of the phenomenon, it can also be obtained for every phase of the cycle.

Unsteady Pressure Distributions

Experiments were made at Mach numbers 0.40, 0.55, 0.75, and 0.85. The vortex street frequency was determined from visualization by measuring the duration between the passing of two successive vortices at a given streamwise position. The Strouhal number maintains a constant value close to 0.20.

The FFT of unsteady pressure signals shows two components at frequencies N and $2N$. The fundamental one, which is consistent with the value obtained from the visualization, is caused by one row of vortices. The first harmonic is due to both rows. Around the greater part of the cylinder, the intensity of the fundamental component appears to be clearly higher than that of the first harmonic. Nevertheless, close to the plane of symmetry, the former decreases strongly and the later becomes dominant. Figure 4 shows examples of spectra at different azimuths and illustrates this phenomenon. Close to stagnation points the first harmonic is dominant, and precisely at stagnation point the fundamental component vanishes. This phenomenon can be explained by the fact that the two vortex rows disturb the flow around the body with a comparable intensity only near the plane of symmetry. Everywhere else, the influence of one vortex predominates. For example, on the upper part of the body, only the upper vortex row effect is significant. This is because the perturbations generated by the lower vortex line must pass around the cylinder or through the recirculating zone. Ac-

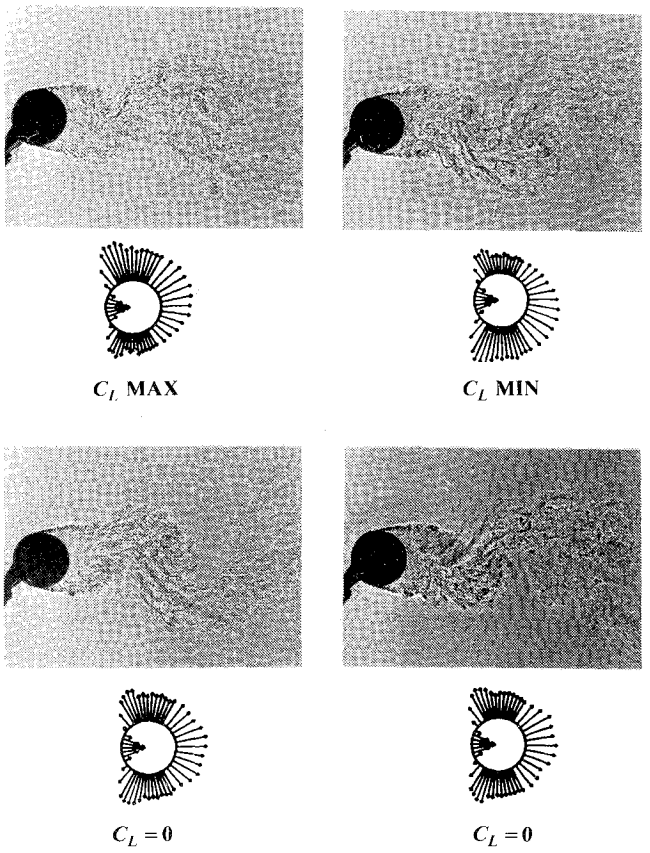

Fig. 9 Flow visualization and pressure coefficient distribution at $M_\infty = 0.40$ (pressure coefficients are measured over the upper part and deduced over the lower part as 180 deg out of phase).

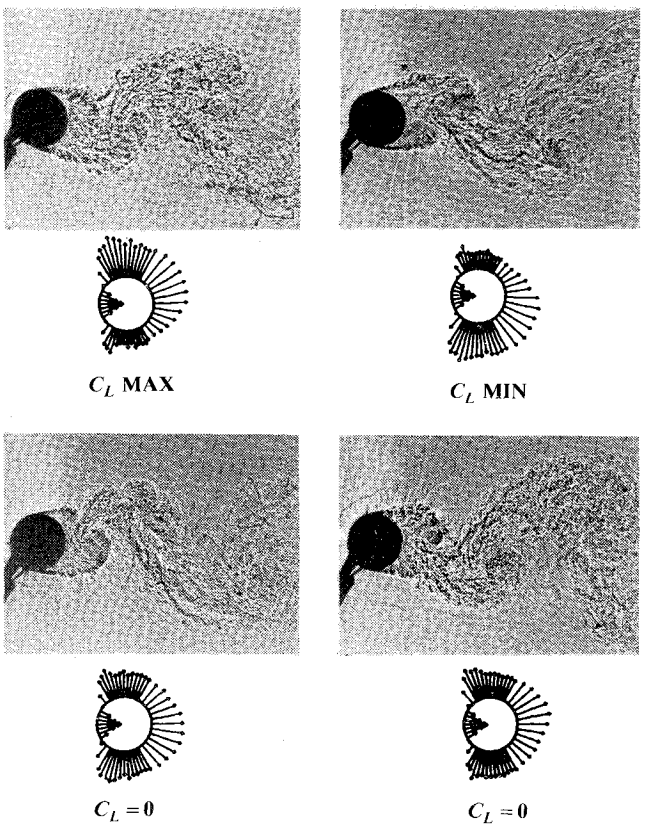

Fig. 10 Flow visualization and pressure coefficient distribution at $M_\infty = 0.55$ (pressure coefficients are measured over the upper part and deduced over the lower part as 180 deg out of phase.)

cording to this interpretation, the fluctuating pressures at frequency $2N$ should be more intense at the rear of the cylinder than close to the front stagnation point because of the proximity of the vortex street. Measurements confirmed this prediction (Fig. 4).

The steady pressure distributions p/p_∞ are given in Fig. 5, together with amplitude A of the fundamental component of the unsteady pressure. It can be seen that A/p_∞ is very low close to the front stagnation point. It then increases at an almost constant value until it reaches the vicinity of the rear stagnation point, at which it decreases slightly. In subsonic flow the unsteady disturbances issuing from the vortex street gradually decrease when approaching the front stagnation point. On the other hand, for $M_\infty = 0.75$ and 0.85 the pressure fluctuations suddenly diminish at an azimuth of about 80 deg. The existing shock waves prevent the downstream perturbations from passing around the cylinder and cause the unsteady pressure intensity to decrease strongly upstream of the farthest limit reached by the separation points (Fig. 8). It can be seen in Fig. 5 that for $M_\infty = 0.55$, 0.75, and 0.85, the level of the unsteady pressure is so high that it cannot be regarded as simply a perturbation field superimposed on the steady mean motion.

Tests were performed to verify the difference in phase between the fluctuating pressures on the lower and upper parts of the body. The movable transducer was fixed at azimuths -30, -20, and -10 deg. For $M_\infty = 0.40$, Fig. 6 shows a difference in phase of about 180 deg for the fundamental component for two symmetrical positions of the transducer. For $M_\infty = 0.55$, we find the same difference in phase, which becomes very perceptible at azimuths ± 30 and ± 20 deg. For $M_\infty = 0.75$, the existence of shock waves makes the measurements less accurate, because the intensity of the perturbations is reduced near the front stagnation point and because the signal-to-noise ratio decreases. We can therefore conclude that the opposition in phase is not perceptible near the front stagnation point. Consequently, the movable transducer was fixed at an azimuth of 190 deg: measurements actually indicated an out-of-phase opposition of 180 deg at the rear of the body. This phenomenon has also been observed by Shang in a numerical resolution of time-dependent, compressible Navier-Stokes equations.[10]

Figure 7 shows that, at every phase during a cycle, the relative unsteady pressure phase is constant over the upper part of the body, except for measurement points close to the plane of symmetry.

For $M_\infty = 0.85$, the shock waves strongly reduced the perturbations near the stagnation point and the noise drowned the fixed transducer signal, making it impossible to determine the fixed signal phase at the initial time and thus synchronize the movable transducer signal.

Unsteady Lift and Drag Coefficients

Drag and lift coefficients were calculated by integrating the measured pressures; the friction contribution was thus omitted. The mean drag coefficient was calculated from pressure tap measurements.

As the fundamental component of the fluctuating pressure is nil at the stagnation points and 180 deg out of phase at the symmetrical points on the cylinder, the unsteady drag component at frequency N is nil. The first harmonic component is also 180 deg out of phase at the symmetrical points, but around the stagnation points its amplitude is not zero.

Table 1 Lift and drag coefficients

M_∞	$\bar{C}_D$	rms C_L	rms C_D
0.40	1.334	0.357	0.48×10^{-2}
0.55	1.455	0.453	0.42×10^{-2}
0.75	1.628	0.251	1.14×10^{-2}

Therefore, only those parts of the cylinder will contribute to the unsteady drag and, consequently, the drag coefficient will be very small.

While the mean lift coefficient is zero, the unsteady lift coefficient has a component at frequency N that is far from negligible.

The mean drag coefficient and the rms values of the lift and drag are listed in Table 1.

If the coupling between the vortex street and the flow over the body can be characterized by the intensity of the unsteady pressure perturbations, the lift coefficient values show that this coupling increases with M_∞ and that its maximum value is attained in the vicinity of the critical Mach number. When compared with computational results obtained by Shang[10] at Reynolds number 1.65×10^5 and Mach number 0.6, the results of this study for both mean drag and unsteady lift coincide very well. In his paper, Shang also notes that the drag coefficient oscillates at a frequency twice as high as that of the lift coefficient.

Thanks to synchronization between pressure and visualization, the pressure distribution on the body can be drawn for every picture. Figure 8 shows a sequence of frames that covers one period of the phenomenon for $M_\infty = 0.75$ as well as the corresponding evolution of the lift coefficient vs time. Figures 9 and 10 show the visualization of the flow and the pressure coefficient distribution for $M_\infty = 0.40$ and 0.55 at the phases when the lift coefficient attains its maximum values. All of these results are consistent and tend to prove that the unsteady pressure on the body is quite well synchronized with the visualization. It can also be observed that the lift coefficient reaches its maximum value whenever the separation point on the lower side of the cylinder is nearest to the front stagnation point; its minimum value occurs at the position of the farthest downstream excursion of the separation point. When the lift coefficient is nil, there exist two configurations for the vortex street that give the same pressure distribution on the cylinder.

Acknowledgments

The author wishes to thank Prof. A. Dyment for his valuable advice and J. P. Flodrops and P. Gryson for their help with the execution of the present study. This research was supported by the French Ministry of Defense (DRET Groupe 6).

References

[1] Farell, C., "Flow Around Fixed Circular Cylinders: Fluctuating Load," *Journal of the Eng. Mech. Div.,* June 1981, p. 565-588.

[2] James, W. D., Paris, S. W., and Malcolm, D. N., "Study of Viscous Crossflow Effects on Circular Cylinders at high Reynolds Numbers," *AIAA Journal,* Vo. 18, Sept. 1980, pp. 935-944.

[3] Roshko, A., "Experiments on the Flow past a Circular Cylinder at very high Reynolds Number," *Journal of Fluid Mechanics,* Vol. 10, 1960, pp. 345-356.

[4] Nauman, A., Morsbach, M., and Kramer, C., "Separated Flow," AGARD CP4, 1966, pp. 539-574.

[5] Murthy, V. S. and Rose, W. C., "Detailed Measurements on a Circular Cylinder in Cross Flow," *AIAA Journal,* Vol. 16, June 1978, pp. 549-550.

[6] Dyment, A., "Vortices Following Two Dimensional Separation," *Vortex Motion,* edited by Hornung and Muller, F. Vieweg & Sohn, Braunschweig, FRG, 1982.

[7] Dyment, A. and Gryson, P., "Etude d'Ecoulements Turbulents Subsoniques et Supercritiques par Visualisation Ultra Rapide," AGARD CP 227, 1979.

[8] Dyment, A., "Vortex Shedding from Bluff Bodies in Oscillatory Flow," Euromech 119, London, 1979.

[9] Dyment, A., Gryson, P., and Ducruet, C., "Unsteady Separation and Reversed Flow in External Fluid Dynamics," Euromech 139, Marseille, 1980.

[10] Shang, J. S., "Oscillatory Compressible Flow Around a Cylinder," AIAA Paper 82-0098, 1982.